

## Differential expression of HCN subunits alters voltage-dependent gating of *h*-channels in CA1 pyramidal neurons from dorsal and ventral hippocampus

Kelly A. Dougherty,<sup>1\*</sup> Daniel A. Nicholson,<sup>2\*</sup> Lauroa Diaz,<sup>1</sup> Eric W. Buss,<sup>2</sup> Krystina M. Neuman,<sup>2</sup> Dane M. Chetkovich,<sup>3,4</sup> and Daniel Johnston<sup>1</sup>

<sup>1</sup>Center for Learning and Memory, The University of Texas at Austin, Austin, Texas; <sup>2</sup>Department of Neurological Sciences, Rush University Medical Center, Chicago, Illinois; <sup>3</sup>Davee Department of Neurology and Clinical Neurosciences, Northwestern University Feinberg School of Medicine, Chicago, Illinois; and <sup>4</sup>Department of Physiology, Northwestern University Feinberg School of Medicine, Chicago, Illinois

Submitted 7 January 2013; accepted in final form 12 January 2013

**Dougherty KA, Nicholson DA, Diaz L, Buss EW, Neuman KM, Chetkovich DM, Johnston D.** Differential expression of HCN subunits alters voltage-dependent gating of *h*-channels in CA1 pyramidal neurons from dorsal and ventral hippocampus. *J Neurophysiol* 109: 1940–1953, 2013. First published January 16, 2013; doi:10.1152/jn.00010.2013.—The rodent hippocampus can be divided into dorsal (DHC) and ventral (VHC) domains on the basis of behavioral, anatomical, and biochemical differences. Recently, we reported that CA1 pyramidal neurons from the VHC were intrinsically more excitable than DHC neurons, but the specific ionic conductances contributing to this difference were not determined. Here we investigated the hyperpolarization-activated current ( $I_h$ ) and the expression of HCN1 and HCN2 channel subunits in CA1 pyramidal neurons from the DHC and VHC. Measurement of  $I_h$  with cell-attached patches revealed a significant depolarizing shift in the  $V_{1/2}$  of activation for dendritic *h*-channels in VHC neurons (but not DHC neurons), and ultrastructural immunolocalization of HCN1 and HCN2 channels revealed a significantly larger HCN1-to-HCN2 ratio for VHC neurons (but not DHC neurons). These observations suggest that a shift in the expression of HCN1 and HCN2 channels drives functional changes in  $I_h$  for VHC neurons (but not DHC neurons) and could thereby significantly alter the capacity for dendritic integration of these neurons.

CA1 pyramidal neuron; dorsal hippocampus; ventral hippocampus; hyperpolarization-activated current; HCN channel

THE RODENT HIPPOCAMPUS can be divided along its longitudinal (septotemporal) axis into dorsal (the dorsal hippocampus, or DHC) and ventral (the ventral hippocampus, or VHC) components on the basis of behavioral, anatomical, and biochemical differences between these two domains (Bannerman et al. 2004; Dong et al. 2009; Fanselow and Dong 2010; Gage and Thompson 1980; Grigoryan et al. 2012; Maggio and Segal 2007; Moser and Moser 1998; van Groen and Wyss 1990). CA1 pyramidal neurons from the DHC and the VHC also exhibit significant differences in their location-dependent firing fields (or place fields), such that place fields become progressively larger along the dorsal-ventral axis toward the VHC (Jung et al. 1994; Maurer et al. 2005). Recently, we reported that CA1 pyramidal neurons from the VHC were intrinsically more excitable than their DHC counterparts. This difference stemmed from a more depolarized resting membrane potential (RMP) and higher input resistance ( $R_{in}$ ) observed in VHC

neurons. Such dorsal-ventral differentiation in membrane properties suggests the potential for significant differences in somatic and dendritic integration between DHC and VHC neurons, which may affect the specificity of place fields along this same axis. The underlying ionic mechanisms for such segregation in intrinsic electrophysiological properties, however, remain unknown.

The hyperpolarization-activated cation nonselective current ( $I_h$ ) is a noninactivating inward current that serves as a key regulator of intrinsic excitability for CA1 pyramidal neurons by influencing both the  $R_{in}$  and the RMP (Pape 1996).  $I_h$  is unevenly distributed along the somatodendritic axis of CA1 pyramidal neurons, such that the density of  $I_h$  is seven to eight times greater in distal stratum radiatum (dSR) than at the soma (Magee 1998). This somatodendritic  $I_h$  gradient shapes excitatory postsynaptic potentials (EPSPs) and influences both their propagation and summation (Magee 1998, 1999, 2000; Robinson and Siegelbaum 2003). The channels responsible for mediating  $I_h$  belong to the hyperpolarization-activated cyclic nucleotide-gated (HCN) family of voltage-gated ion channels. Although four HCN channel subunits have been identified, only HCN1 and HCN2 are expressed in CA1 pyramidal neurons in adult rats (Robinson and Siegelbaum 2003). Native *h*-channels are presumed to be heterotetramers comprised of HCN1 and HCN2 subunits with biophysical properties intermediate to those of homotetrameric HCN1 and HCN2 channels (Chen et al. 2001; Robinson and Siegelbaum 2003; Ulens and Tytgat 2001). Similar to the gradient of  $I_h$  density, HCN1 and HCN2 immunoreexpression levels along the somatodendritic axis exhibit distal enrichment in CA1 pyramidal neurons (Lörincz et al. 2002; Notomi and Shigemoto 2004). However, the biophysical properties of  $I_h$  and the expression of HCN1 and HCN2 channel subunits across the dorsal-ventral hippocampal axis remain largely unexplored.

Layer II stellate neurons from the medial entorhinal cortex (MEC) also show location-dependent firing fields (grid fields; Fyhn et al. 2004; Hafting et al. 2005). Similar to the place fields of CA1 pyramidal neurons along the dorsal-ventral axis, grid fields become progressively larger toward the ventral boundary of the MEC, a feature that has been partially attributed to an intercellular gradient of  $I_h$  along this same axis of the MEC (Brun et al. 2008; Garden et al. 2008; Giocomo and Hasselmo 2009; Hafting et al. 2005). Here we hypothesized that similar organizing principles may exist for CA1 pyramidal neurons and investigated the functional properties of  $I_h$  and the

\* K. A. Dougherty and D. A. Nicholson contributed equally to this work.

Address for reprint requests and other correspondence: K. A. Dougherty, Center for Learning and Memory, Univ. of Texas at Austin, 100 East 24th St., Rm. 2.310, Austin, TX 78712 (e-mail: kelly@mail.clm.utexas.edu).

expression of HCN channel subunits across the dorsal-ventral hippocampal axis. Briefly, we found that the somatodendritic *h*-conductance gradient was functionally augmented by a distance-dependent depolarizing shift in the midpoint of the conductance-voltage (*G*-*V*) relationship for *h*-channels from VHC, but not DHC, neurons. This functionally augmented *h*-conductance gradient was paralleled by a distance-dependent shift in the ratio of HCN1-to-HCN2 channel subunit expression for VHC, but not DHC, neurons. Together, these results suggest that differential HCN channel subunit expression across the dorsal-ventral hippocampal axis drives functional changes in the biophysical properties of *h*-channels, which could thereby significantly alter the capacity for dendritic integration of these neurons.

## MATERIALS AND METHODS

**Hippocampal slice preparation.** Transverse, acute hippocampal slices (350  $\mu$ m) were prepared from 4- to 8-wk-old male Sprague-Dawley rats according to protocols reviewed and approved by the University of Texas at Austin Institutional Animal Care and Use Committee. DHC and VHC slices were prepared as previously described (Dougherty et al. 2012), transferred to a holding chamber containing holding saline composed of (in mM) 125 NaCl, 2.5 KCl, 1.25 NaH<sub>2</sub>PO<sub>4</sub>, 25 NaHCO<sub>3</sub>, 2 CaCl<sub>2</sub>, 2 MgCl<sub>2</sub>, 12.5 dextrose, 1.3 ascorbic acid, and 3 sodium pyruvate, continuously bubbled with 95% O<sub>2</sub>-5% CO<sub>2</sub>, incubated for 15 min at  $\sim$ 35°C, and then allowed to rest at room temperature for at least 45 min prior to recording.

**Electrophysiology.** Whole cell current-clamp recordings were performed on CA1 pyramidal neurons with a Dagan BVC-700A amplifier (Dagan, Minneapolis, MN) and Axograph X data acquisition software (Axograph, Canberra, Australia). Signals were low-pass filtered at 3 kHz and sampled at 10 kHz with an ITC-18 computer interface (InstruTech, Port Washington, NY). Slices were continuously perfused with artificial cerebrospinal fluid (aCSF) of the following composition (in mM): 125 NaCl, 3 KCl, 1.25 NaH<sub>2</sub>PO<sub>4</sub>, 25 NaHCO<sub>3</sub>, 2 CaCl<sub>2</sub>, 1 MgCl<sub>2</sub>, 12.5 dextrose, 1.3 ascorbic acid, and 3 sodium pyruvate, continuously bubbled with 95% O<sub>2</sub>-5% CO<sub>2</sub>. All current-clamp recordings were performed in an aCSF supplemented with 20  $\mu$ M DNQX, 50  $\mu$ M D,L-APV, and 2  $\mu$ M gabazine (Ascent Scientific, Princeton, NJ). Electrodes were filled with an internal solution of the following composition (in mM): 120 K-gluconate, 20 KCl, 10 HEPES, 4 NaCl, 4 Mg-ATP, 0.3 Na-GTP, and 7 K<sub>2</sub>-phosphocreatine, pH = 7.3 adjusted with KOH. Neurobiotin (Vector Laboratories, Burlingame, CA) was added to the pipette solution (0.1–0.2%) in order to facilitate later visualization of individual neurons. All voltages have been corrected for a measured liquid junction potential (LJP) of 8 mV. Experiments were terminated if the series resistance exceeded 30 M $\Omega$ . The whole cell electrophysiological experiments presented in this study were performed concomitantly with the whole cell current-clamp experiments presented by Dougherty et al. (2012). All experiments for this and the following section were performed at 32–34°C.

**Cell-attached voltage-clamp recordings.** Slices were perfused with oxygenated aCSF as indicated above, and dendritic cell-attached patches were formed with the following extracellular (pipette) solution (in mM): 100 KCl, 20 NaCl, 20 TEA-Cl, 10 HEPES, 5 EGTA, 5 4-AP, 1 MgCl<sub>2</sub>, 3 BaCl<sub>2</sub>, 1 NiCl<sub>2</sub>, 0.5 CdCl<sub>2</sub>, and 0.001 TTX, brought to a pH of 7.4 with TEA-OH. Currents were measured with an Axopatch 200B amplifier (Axon Instruments, Foster City, CA) controlled by Axograph X data acquisition software, low-pass filtered at 2 kHz, and sampled at 10 kHz with an ITC-18 computer interface (InstruTech). *I<sub>h</sub>* was elicited by 500-ms step hyperpolarizations from a holding potential that was 20 mV more positive than RMP in  $-10$ -mV increments ( $-20$ -mV increments for somatic recordings) ranging from  $+10$  to  $-90$  mV (relative to RMP). Passive leak and

capacitive transients were subtracted off-line with a scaled leak trace elicited by 10-mV depolarizations from the holding potential. Typically, between 100 and 220 individual leak traces were averaged in order to minimize the addition of noise to the leak-subtracted current waveforms. To minimize errors associated with cell-attached patches exhibiting large noninactivating currents, dendritic recordings with currents large enough to cause an appreciable voltage error [as defined by independent measurement of the *R<sub>in</sub>* (at RMP) for each somatodendritic recording location] were discarded (Williams and Wozny 2011). These *R<sub>in</sub>* (at RMP) values were reported by Dougherty et al. (2012). The RMP for cell-attached patches was determined immediately upon breaking in. However, this membrane potential was highly variable and difficult to determine accurately, so all reported membrane potentials were standardized to the average RMP determined from stable whole cell current-clamp recordings at similar somatodendritic locations unless stated otherwise. These values were corrected for the relevant LJP and were reported by Dougherty et al. (2012). Membrane potentials were adjusted by an additional  $-1$  mV in order to correct for the LJP measured between the external (pipette) solution and the aCSF. The surface area of free membrane within the pipette was determined for individual patches as described by Sakmann and Neher (1995).

**Serial section preembedding silver-intensified ultrasmall immunogold electron microscopy.** Hippocampal tissue from six male Sprague-Dawley rats (8–10 wk old) was prepared as previously described (Lewis et al. 2011; Wilkars et al. 2012) but cut following the angular approaches used in patch-clamp slice preparation to isolate dorsal and ventral hippocampal CA1. Rats (8–10 wk old) were perfused with 60 ml of room temperature physiological saline, followed by 200 ml of ice-cold sodium acetate buffer containing 2% paraformaldehyde-1% glutaraldehyde (pH = 6.0) and then 1,000 ml of ice-cold sodium borate buffer containing 2% paraformaldehyde-1% glutaraldehyde (pH = 9.0). Brains were removed, hemisected, cut to isolate dorsal and ventral hippocampus, and sectioned on a vibratome to produce 70- $\mu$ m-thick slices approximately in the transverse orientation. Slices were rinsed in Tris-buffered saline (TBS) followed by 1% NaBH<sub>4</sub>, rinsed again in TBS, blocked with 10% normal goat serum (NGS) in TBS, and incubated at 4°C overnight in antibodies against either guinea pig anti-HCN1 or anti-HCN2 at 1:1,000 in TBS + 2% NGS + 0.1% Triton X-100. Slices were then rinsed in incubation buffer followed by TBS, blocked with TBS + 2% NGS + 1% bovine serum albumin (BSA) + 0.3% coldwater fish skin gelatin, and then incubated in goat anti-guinea pig ultrasmall immunogold particles at a dilution of 1:100 (Aurion, Electron Microscopy Sciences, Hatfield, PA) in the blocking solution with acetylated BSA replacing BSA for 48 h at 4°C. Slices were rinsed in incubation buffer followed by TBS and then phosphate-buffered saline (PBS) and fixed with 2% glutaraldehyde in PBS. Silver enhancement followed, using the R-Gent SE-EM Enhancement Kit (Aurion), with a developer-to-enhancer ratio of 1:10. Slices were osmicated in 0.4% OsO<sub>4</sub> in PBS for 8 min, rinsed, stained en bloc with 1% aqueous uranyl acetate, rinsed, dehydrated, and flat-embedded in Araldite 502. Polymerized slivers of CA1 were then dissected from slices, reembedded, and rotated 90° for thin sectioning, such that each ultrathin section contained the two surfaces of the slices cut by the vibratome, and thus directly exposed to the reagents.

Electron micrographs of serial sections (20–35 sections) were obtained at  $\times 7,500$  magnification with a JEOL 1200EX transmission electron microscope (JEOL, Peabody, MA) and always included the “edge” of each section, enabling the analyses to be limited to portions of tissue between  $\sim 2$   $\mu$ m and 10  $\mu$ m from the cut surface. Each serial section spanned the entire extent of CA1, from the alveus to the outer molecular layer of the dentate gyrus, beyond the hippocampal fissure. Fields photographed in the electron microscope were confirmed by taking a picture of the “beam burn” and matching it to histological sections. The fields from which micrographs were obtained were the stratum pyramidale, the proximal 80  $\mu$ m of stratum radiatum (pSR),

and the stratum lacunosum-moleculare (SLM), identified by an abrupt decrease in large-diameter apical dendrites and a band of myelinated fibers running perpendicular to the axis of the apical dendrites. Immunopositive dendrites that were sectioned transversely in each series were then labeled on each micrograph, with their surface area being estimated as the product of the summed circumference of their plasma membranes in each section and the average section thickness (61 nm, determined with Small's methods of minimal folds). Immunogold particles within 20 nm of the membrane were considered to be membrane bound, and those within the cytoplasm were considered to be cytoplasmic. Average particle density is expressed as the total number of membrane-bound particles divided by the total dendritic surface area for each dendrite through its profile in serial sections. Dendritic diameter was determined as the average of measurements obtained from three individual sectional profiles for each dendrite. Only particles projected onto the dendritic membrane were included in the average membrane-bound particle density estimates, since the vast majority of immunoreactivity was dendritic (see also Lörincz et al. 2002).

**Western blots.** Five male Sprague-Dawley rats (8–12 wk old) were anesthetized with isoflurane and transcardially perfused, until the perfusate was clear of red blood cells, with ice-cold oxygenated sucrose-based aCSF containing the following (in mM): 210 sucrose, 1.25  $\text{NaH}_2\text{PO}_4$ , 25  $\text{NaHCO}_3$ , 0.5  $\text{CaCl}_2$ , 7  $\text{MgCl}_2$ , 7 dextrose, 1.3 ascorbic acid, and 3 sodium pyruvate. The brain was immediately removed, hemisected, and cut along its lateral-caudal or dorsal-caudal surface to isolate the dorsal and ventral hippocampus, respectively. Brains were mounted on their cut surfaces and sliced at 300  $\mu\text{m}$  in oxygenated sucrose-based aCSF with a Microm 650V oscillating slicer (ThermoFisher Scientific, Waltham, MA) at 4°C. Slices were immediately frozen over dry ice, after which the CA1 region was microdissected and immediately stored at  $-80^\circ\text{C}$  until use. Tissue was homogenized in lysis buffer containing (in mM) 50 Tris-HCl, pH 7.4, 150 NaCl, 1% Nonidet P-40, 0.1% SDS, 0.5% sodium desoxycholate, 5 EDTA, and a mixture of protease inhibitors (Roche, Basel, Switzerland). Homogenates were centrifuged at 13,000 rpm for 12 min at 4°C, and supernatant was collected. Protein concentrations were determined with a Bradford assay. Supernatant was mixed with sample buffer and heated at 100°C for 5 min, cooled to room temperature, and then resolved on a 10% SDS-PAGE gel at 170 V. Proteins were blotted on a PVDF membrane with semidry transfer conditions. Upon transfer, membranes were blocked in 5% milk in TBS with 0.1% Tween 20 (TBST) for 2 h at room temperature and then incubated in primary antibody (guinea pig anti-HCN1 at 1:1,000 or guinea pig anti-HCN2 at 1:1,000) with 5% milk in TBST at 4°C overnight. Membranes were then rinsed in TBST for  $3 \times 10$  min and incubated in an HRP-conjugated secondary antibody (ThermoFisher Scientific) for 1 h. Antibodies were detected with a SuperSignal West Pico Chemiluminescent kit (ThermoFisher Scientific). Multiple film exposures were collected for each blot, and nonsaturated films were scanned and analyzed with National Institutes of Health ImageJ software. Quantification of band intensity was performed with  $\alpha$ -tubulin (1:5,000; mouse anti- $\alpha$ -tubulin, Santa Cruz Biotechnology, Santa Cruz, CA) as a loading control. Protein load was determined by densitometry and normalized to tubulin. These ratios were then compared with a multivariate analysis of variance (MANOVA), with HCN1/HCN2 and dorsal/ventral as factors.

**Data analysis and statistical evaluations.** The somatic  $R_{in}$  was measured as the slope of the linear portion of the voltage-current plot constructed from the steady-state voltage response to step current injections ranging from  $-50$  pA to 50 pA. The rebound slope ( $RS$ ) was determined from the voltage responses to a family of 800-ms hyperpolarizing step current injections ranging from  $-200$  pA to 0 pA in 20-pA increments. The  $RS$  was defined as the slope of the linear fit of the rebound amplitude vs. steady-state membrane potential plot (Brager and Johnston 2007). The resonance frequency ( $f_R$ ) was determined from the voltage response to the Chirp20 current stimulus. This

stimulus consisted of a modulated sine wave of constant amplitude (50 pA). The frequency of this sine wave was increased linearly at a rate of 1 Hz/s for 20 s. The impedance amplitude was calculated from the ratio of the fast Fourier transforms of the voltage responses and current stimuli, and the  $f_R$  was defined as the frequency associated with the peak impedance value. The resonance strength ( $Q$ ) was defined as the ratio of the maximal impedance value and the impedance at 0.5 Hz. Normalized  $G$ - $V$  relationships were described assuming a Boltzmann function:  $G(V) = I/[1 + e^{(V-V_{0.5})/k}]$ , where  $G(V)$  is the normalized conductance,  $V$  is the membrane potential,  $V_{0.5}$  (or  $V_{1/2}$ ) is the membrane potential associated with one-half of the maximal conductance value, and  $k$  is the slope factor. This slope factor was converted to an electrical valence,  $z$ , according to the relationship  $k = k_B T / z e_0$ , where  $k_B$  is Boltzmann's constant,  $e_0$  is the elementary charge, and  $T$  is the temperature. The time course of activation was described assuming a double-exponential function of the form  $I(t) = I_0 + A_{fast} \exp[-(t - t_0)/\tau_{fast}] + A_{slow} \exp[-(t - t_0)/\tau_{slow}]$ , where  $I_0$  and  $t_0$  are constants for the offsetting the fit along the current and time axes,  $\tau_{fast}$  and  $\tau_{slow}$  are the fast and slow time constants, and  $A_{fast}$  and  $A_{slow}$  are their respective amplitudes. The time course of deactivation was described assuming a similar function of the form  $I(t) = I_0 - A_{deact} \exp[-(t - t_0)/\tau_{deact}]$ , where  $\tau_{deact}$  is the time constant of deactivation and  $A_{deact}$  is its amplitude. The voltage dependences of  $\tau_{fast}$  and  $\tau_{deact}$  were described by an exponential function of the form  $\tau(V) = 1/A_0 \exp(z_x e_0 V / k_B T)$ , where  $A_0$  is the rate constant at 0 mV and  $z_x$  is the electrical valence associated with either  $\tau_{fast}$  or  $\tau_{deact}$  (all other parameters have their aforementioned meanings).

The statistical significance of whole cell current-clamp and cell-attached voltage-clamp data was evaluated between data sets consisting of two independent groups with the Student's  $t$ -test. Wilcoxon's rank sum test was applied when one or both group(s) had an  $n < 7$ , data were not normally distributed, or the variances were unequal. Wilcoxon's signed-rank test was used to evaluate differences between the paired recordings in the 500- and 100-ms time frames. All hypothesis testing was performed with  $\alpha = 0.05$ . Statistical evaluations were performed with IGOR Pro v6.11 (IGOR Pro, Lake Oswego, OR).

For immunogold electron microscopy (EM) experiments, immunoreactivity was compared statistically with a multivariate analysis of covariance (MANCOVA), with HCN1/HCN2, dorsal/ventral, and proximal/distal as factors and dendritic diameter as covariate (Statistica, StatSoft, Tulsa, OK). There were no statistically significant differences in particle density between dendrites 2–5  $\mu\text{m}$  and 5–10  $\mu\text{m}$  from the cut surface, so all dendrites from each series were pooled. Membrane-bound particle density data from somata were compared statistically to each other, but not to dendrites, with a MANOVA, with HCN1/HCN2 and dorsal/ventral as factors. For somatic analyses, mosaics of adjacent electron micrographs in two to four serial sections were tiled to obtain fields containing two to four somata, presumed to be CA1 pyramidal neurons on the basis of their diameter ( $\sim 15$   $\mu\text{m}$ ) and the presence of masses of heterochromatin in their nucleoli. Particle densities for somata are based on the aggregate membrane surface area present in the electron micrographs, estimated as the product of linear length of membrane and section thickness. Data were obtained from 852 immunopositive dendrites in SLM, 180 immunopositive dendrites in pSR, and 28 immunopositive somata. The total surface area of the dendrites analyzed was 2,471  $\mu\text{m}^2$  in SLM and 422  $\mu\text{m}^2$  in pSR, and total somatic surface area was 142  $\mu\text{m}^2$ . Three-dimensional reconstructions were rendered in Reconstruct (<http://synapses.clm.utexas.edu/tools/reconstruct/reconstruct.stm>).

## RESULTS

**Pharmacological evidence for  $I_h$  in DHC and VHC neurons.** As an initial evaluation of the relative contribution of  $I_h$  to the intrinsic electrophysiological properties of DHC and VHC

neurons, the  $I_h$  blocker ZD7288 (10  $\mu\text{M}$ ) was washed into the recording chamber while RMP was monitored with a somatic recording electrode in the whole cell configuration (Fig. 1A). RMP was monitored every 30 s and clearly hyperpolarized for both DHC and VHC neurons in response to 10  $\mu\text{M}$  ZD7288 wash-in (Fig. 1B). Although the RMPs for DHC and VHC neurons were significantly different before 10  $\mu\text{M}$  ZD7288 wash-in (DHC  $-74.0 \pm 1.6$  mV, VHC  $-67.9 \pm 1.5$  mV), they were no longer significantly different after 10  $\mu\text{M}$  ZD7288 wash-in (DHC  $-78.8 \pm 1.7$  mV, VHC  $-75.7 \pm 2.0$  mV; Fig. 1C). Furthermore, the magnitude of the hyperpolarization of RMP following 10  $\mu\text{M}$  ZD7288 wash-in was significantly greater for VHC neurons than DHC neurons (DHC  $-4.8 \pm 0.9$  mV, VHC  $-7.8 \pm 1.2$  mV; Fig. 1D), suggesting that  $I_h$  has a stronger influence over the RMP of VHC neurons than DHC neurons.

The  $R_{in}$  measured from a common potential [ $R_{in}$  (at  $-73$  mV)] was also monitored before and after 10  $\mu\text{M}$  ZD7288 wash-in (Fig. 1E).  $R_{in}$  (at  $-73$  mV) was significantly higher for VHC neurons before wash-in (DHC  $56.6 \pm 5.0$  M $\Omega$ , VHC  $70.5 \pm 6.4$  M $\Omega$ ) and remained significantly higher after wash-in (DHC  $104.2 \pm 6.9$  M $\Omega$ , VHC  $141.9 \pm 4.0$  M $\Omega$ ), although  $R_{in}$  (at  $-73$  mV) clearly increased for both DHC and VHC neurons in response to 10  $\mu\text{M}$  ZD7288 wash-in (Fig. 1, E–G). The magnitude of the increase in the  $R_{in}$  (at  $-73$  mV) was, however, significantly larger for VHC neurons than DHC neurons (DHC  $47.7 \pm 8.0$  M $\Omega$ , VHC  $71.3 \pm 4.4$  M $\Omega$ ; Fig.

1G). This significant residual difference was observed at all membrane potentials tested and suggests that factors other than  $I_h$  also contribute to the difference in somatic  $R_{in}$  (Fig. 1F). In a previous study, we reported significant morphological differences between DHC and VHC neurons that could, in principle, contribute to the observed differences in somatic  $R_{in}$  (Dougherty et al. 2012). However, another likely source for this residual difference in  $R_{in}$  could be the presence of an additional resting conductance in DHC neurons (e.g., a potassium conductance). The basis for this remaining fixed difference in  $R_{in}$  between DHC and VHC neurons was not examined further.

*Indirect electrophysiological evidence for  $I_h$  in DHC and VHC neurons.* Indirect evidence of  $I_h$  can be obtained with the whole cell current-clamp method by employing electrophysiological protocols designed to elicit voltage responses uniquely associated with  $I_h$ . Specifically, the  $RS$ , which quantifies the characteristic voltage sag and rebound profile associated with  $I_h$  activation and deactivation in response to step hyperpolarizing current injections, and the  $f_R$ , which accounts for the high-pass filtering quality associated with  $I_h$ , were used as indirect indicators for the presence of  $I_h$  in DHC and VHC neurons (see MATERIALS AND METHODS). These parameters were particularly good indicators of  $I_h$  because of their elimination in the presence of ZD7288. The  $RS$  was determined from the voltage responses to a family of 800-ms hyperpolarizing somatic step current injections starting from either RMP [ $RS$  (at RMP)] or a common membrane potential [ $RS$  (at  $-73$  mV)];

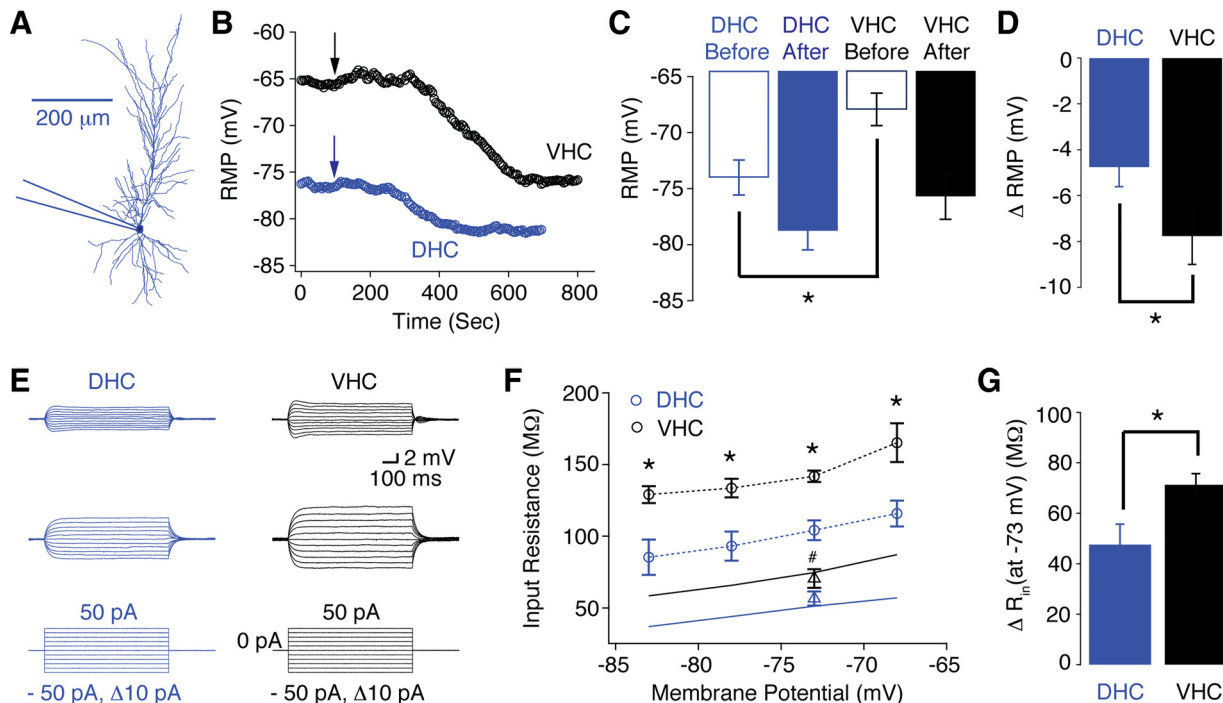


Fig. 1. Pharmacological evidence for hyperpolarization-activated current ( $I_h$ ) in dorsal (DHC) and ventral (VHC) hippocampal neurons. *A*: morphological reconstruction of a DHC CA1 pyramidal neuron depicting the somatic recording location for the data presented in this figure. *B*: resting membrane potential (RMP) was monitored over time as 10  $\mu\text{M}$  ZD7288 was washed in for representative DHC and VHC neurons. Arrows indicate the approximate time when 10  $\mu\text{M}$  ZD7288 was added to the perfusion system. *C*: RMP was significantly more depolarized for VHC neurons than DHC neurons before (Wilcoxon rank sum test,  $*P < 0.05$ ) but not after (Wilcoxon rank sum test,  $P > 0.05$ ) 10  $\mu\text{M}$  ZD7288 wash-in. *D*: the change ( $\Delta$ ) in RMP in response to 10  $\mu\text{M}$  ZD7288 wash-in was significantly larger for VHC neurons than DHC neurons (Wilcoxon rank sum test,  $*P < 0.05$ ). *E*: voltage responses to 800-ms somatic step current injections starting from  $-73$  mV for DHC and VHC neurons before (*top*) and after (*bottom*) 10  $\mu\text{M}$  ZD7288 wash-in. *F*: in the presence of 10  $\mu\text{M}$  ZD7288, input resistance ( $R_{in}$ ) was significantly larger for VHC neurons than DHC neurons at all tested membrane potentials (Wilcoxon rank sum tests, all  $*P < 0.05$ ; for voltages other than  $-73$  mV,  $n = 3$ ). Open triangles represent  $R_{in}$  (at  $-73$  mV) before 10  $\mu\text{M}$  ZD7288. Solid lines represent the voltage dependence of the somatic  $R_{in}$  in the absence of 10  $\mu\text{M}$  ZD7288 (data from Dougherty et al. 2012). *G*: the change in  $R_{in}$  (at  $-73$  mV) in response to 10  $\mu\text{M}$  ZD7288 wash-in was significantly larger for VHC neurons than DHC neurons (Wilcoxon rank sum test,  $*P < 0.05$ ). Unless otherwise stated,  $n = 5$  for both DHC and VHC neurons.

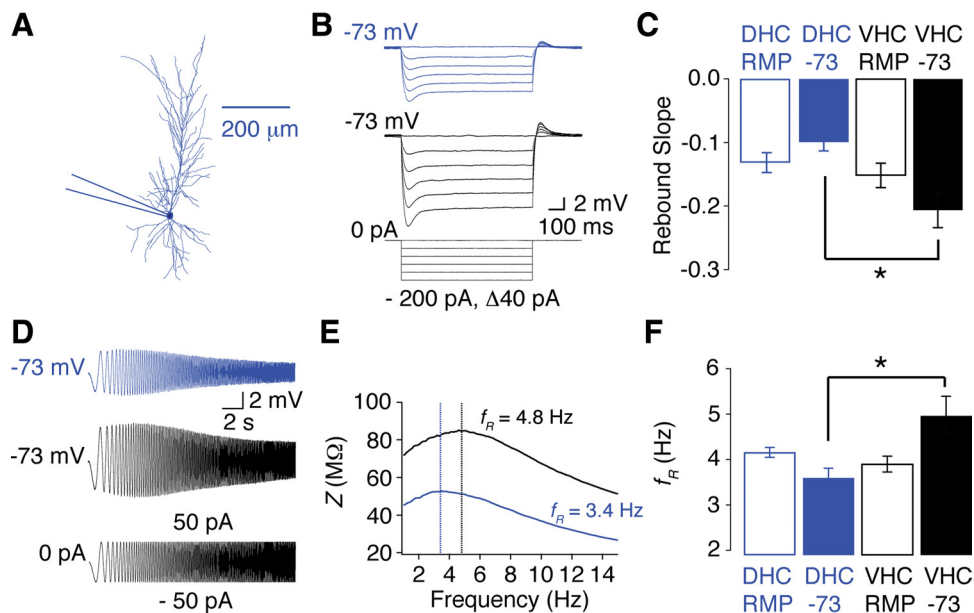


Fig. 2. Indirect electrophysiological evidence for  $I_h$  in DHC and VHC neurons. *A*: morphological reconstruction of a DHC CA1 pyramidal neuron depicting the somatic recording location for the data presented this figure. *B*: voltage responses for DHC (blue traces) and VHC (black traces) neurons elicited from  $-73$  mV in response to 800-ms step current injections ranging from  $-200$  pA to  $0$  pA in 40-pA increments. *C*: the rebound slope ( $RS$ ) (at  $-73$  mV) was significantly more negative in VHC neurons than DHC neurons (Student's  $t$ -test,  $*P < 0.05$ ), whereas the  $RS$  (at RMP) was not significantly different (Wilcoxon rank sum test,  $P > 0.05$ ). *D*: voltage responses for DHC (blue traces) and VHC (black traces) neurons elicited from  $-73$  mV in response to the Chirp20 stimulus (see MATERIALS AND METHODS). *E*: impedance amplitude ( $Z$ ) profiles for traces in *D*. Vertical dashed lines indicate the resonance frequency ( $f_R$ ) for the DHC (blue) and VHC (black) neurons, respectively. *F*: the  $f_R$  (at  $-73$  mV) was significantly higher in VHC than DHC (Student's  $t$ -test,  $*P < 0.05$ ) neurons, whereas  $f_R$  (at RMP) was not significantly different (Wilcoxon rank sum test,  $P > 0.05$ ).  $n$  Values are listed in Table 1.

Fig. 2*B*]. The  $RS$  (at  $-73$  mV) was significantly more negative for VHC neurons (consistent with greater  $I_h$ ) than DHC neurons (DHC  $-0.10 \pm 0.01$ , VHC  $-0.21 \pm 0.03$ ), whereas the  $RS$  (at RMP) was not significantly different (DHC  $-0.13 \pm 0.02$ , VHC  $-0.15 \pm 0.02$ ; Fig. 2*C*, Table 1). This latter observation likely stems from the difference in RMP between DHC and VHC neurons (Fig. 1*C*) and the voltage dependence of  $I_h$  (see DISCUSSION). Voltage responses elicited by the Chirp20 current stimulus were transformed into impedance values and used to determine the  $f_R$  for DHC and VHC neurons (Fig. 2, *D* and *E*). The  $f_R$  was defined as the frequency associated with the peak impedance value on the impedance amplitude profile (Fig. 2*E*) and was determined for voltage responses elicited by Chirp20 current stimuli starting from RMP [ $f_R$  (at RMP)] and a common membrane potential [ $f_R$  (at  $-73$  mV)]. The  $f_R$  (at  $-73$  mV) was significantly higher for VHC neurons (consistent with greater  $I_h$  in VHC neurons) than DHC neurons (DHC  $3.6 \pm 0.2$ , VHC  $5.0 \pm 0.4$ ), whereas the  $f_R$  (at RMP) was not significantly different (DHC  $4.2 \pm 0.1$ , VHC  $4.0 \pm 0.2$ ; Fig. 2*F*, Table 1).  $Q$  (see MATERIALS AND METHODS) was also larger for VHC neurons than DHC neurons when measured from a common membrane potential [ $Q$  (at  $-73$  mV); DHC  $1.10 \pm 0.03$ , VHC  $1.24 \pm 0.03$ ] but was not

significantly different when measured from RMP [ $Q$  (at RMP); DHC  $1.11 \pm 0.03$ , VHC  $1.16 \pm 0.03$ ; Table 1]. Together, these data provide indirect electrophysiological evidence suggesting that  $I_h$  is greater in VHC neurons than DHC neurons.

**Functional properties of h-channels from DHC and VHC neurons.** The data obtained from whole cell current-clamp experiments described above are consistent with the hypothesis that  $I_h$  is greater in VHC neurons than DHC neurons. However, measurements of  $I_h$  based on whole cell current-clamp data are indirect and can be significantly distorted by differences in the electrotonic structure of the neuron. Therefore, we measured  $I_h$  directly, using the cell-attached voltage-clamp method (Figs. 3–5).  $I_h$  was elicited in dendritic patches (200–300  $\mu$ m from the soma) by 500-ms step hyperpolarizations ranging from  $-90$  to  $20$  mV in  $-10$ -mV increments (all experimental membrane potentials were relative to RMP) from a holding potential  $20$  mV depolarized to RMP (Fig. 3*A*).  $G$ - $V$  relationships determined from the normalized peak tail current (tail- $G$ - $V$  relationship; Fig. 3*A*, insets) were significantly more depolarized for VHC than DHC patches (DHC  $V_{1/2} = -112.5 \pm 1.1$  mV, VHC  $V_{1/2} = -95.0 \pm 2.0$  mV,  $n = 7$ ; Fig. 3, *B* and *C*). The slope factor ( $k$ ) and maximal conductance density ( $G$  density), however, were not significantly different [DHC  $k =$

Table 1.  $I_h$ -related indirect electrophysiological parameters

	$f_R$ at RMP, Hz	$f_R$ at $-73$ mV, Hz	$Q$ at RMP, M $\Omega$ /M $\Omega$	$Q$ at $-73$ mV, M $\Omega$ /M $\Omega$	$RS$ at RMP, mV/mV	$RS$ at $-73$ mV, mV/mV
DHC	$4.2 \pm 0.1$ (12)	$3.6 \pm 0.2^a$ (15)	$1.11 \pm 0.03$ (12)	$1.10 \pm 0.03^b$ (11)	$-0.13 \pm 0.02$ (12)	$-0.10 \pm 0.01^c$ (15)
VHC	$4.0 \pm 0.2$ (6)	$5.0 \pm 0.4^a$ (8)	$1.16 \pm 0.03$ (6)	$1.24 \pm 0.03^b$ (8)	$-0.15 \pm 0.02$ (4)	$-0.21 \pm 0.03^c$ (8)

Values are means  $\pm$  SE for  $n$  values in parentheses. Resonance frequency ( $f_R$ ), resonance strength ( $Q$ ), and rebound slope ( $RS$ ) from dorsal (DHC) and ventral (VHC) hippocampal neurons were tabulated.  $I_h$ , hyperpolarization-activated current. Statistical significance was determined with either a Student's  $t$ -test or the Wilcoxon rank sum test with  $P < 0.05$  (see MATERIALS AND METHODS). Paired superscripted letters indicate significant differences between DHC neurons and VHC neurons.

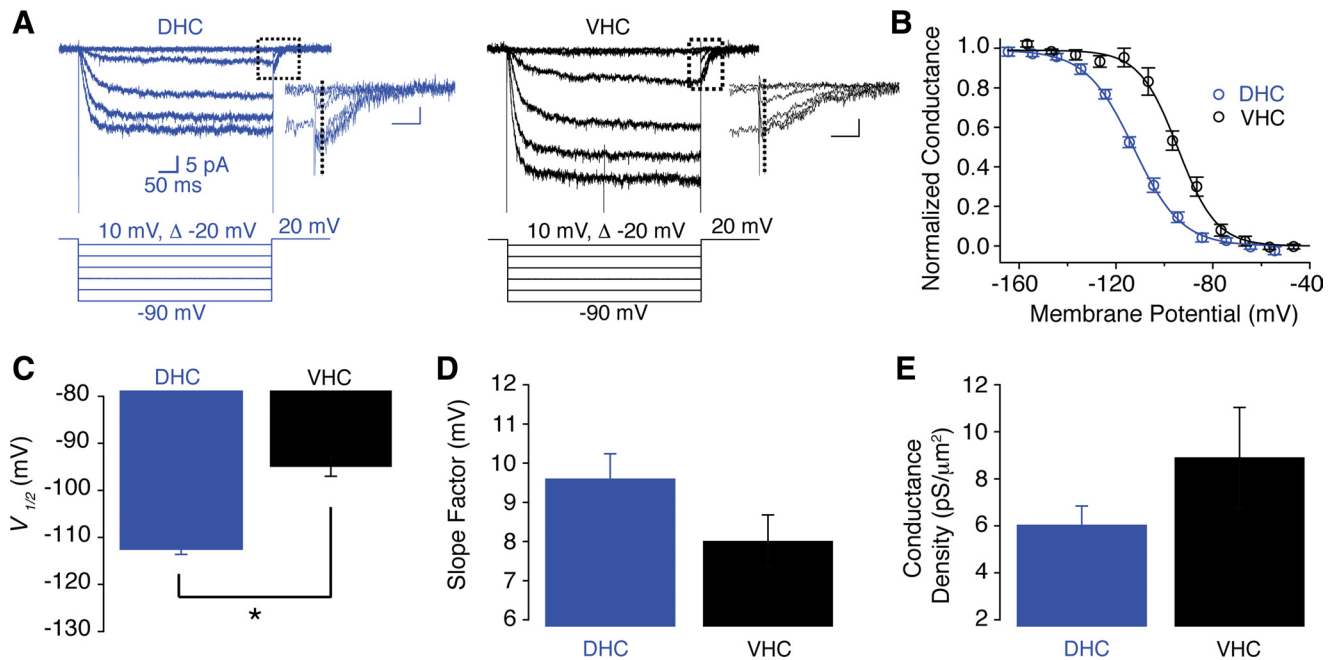


Fig. 3. Voltage-dependent gating of *h*-channels from DHC and VHC neurons. *A*: currents evoked from DHC (left) and VHC (right) dendrites by 500-ms hyperpolarizing voltage steps from a holding potential 20 mV more positive than RMP. The dendritic recording location of these patches was ~220  $\mu$ m from the soma. *Insets*: close-up view of tail currents from the area bounded by the black dotted rectangles. Black vertical dashed lines indicate the approximate location for determining the peak tail current. Vertical scale bars represent 2 pA (DHC, left) and 4 pA (VHC, right), and horizontal scale bars represent 10 ms. *B*: the voltage dependence of activation determined from tail currents was described assuming a Boltzmann function with the following fit parameters: DHC membrane potential for 1/2 maximal conductance ( $V_{1/2}$ ) = -113 mV, slope factor ( $k$ ) = 9.7 mV; VHC  $V_{1/2}$  = -95 mV,  $k$  = 7.9 mV. *C–E*: the  $V_{1/2}$  value of the tail conductance-voltage ( $G$ - $V$ ) relationship (*C*) was significantly more depolarized for *h*-channels from VHC dendrites than DHC dendrites (Student's *t*-test, \* $P$  < 0.05), whereas the slope factor (*D*) and maximal conductance density (*E*) were not significantly different (slope factor: Student's *t*-test,  $P$  > 0.05; maximal conductance density: Student's *t*-test,  $P$  > 0.05). *n* Values are listed in Table 2.

$9.6 \pm 0.6$  mV ( $n = 11$ ),  $G$  density =  $6.0 \pm 0.8$  pS/ $\mu$ m<sup>2</sup> ( $n = 12$ ); VHC  $k = 8.0 \pm 0.7$  mV ( $n = 7$ ),  $G$  density =  $8.9 \pm 2.1$  pS/ $\mu$ m<sup>2</sup> ( $n = 6$ ); Fig. 3, *D* and *E*, Table 2]. Control experiments in which the duration of the step hyperpolarization was extended to 1,000 ms did not show any significant differences in voltage-dependent activation or kinetics when compared with the 500-ms time frame (data not shown). Moreover, similar results were observed when RMP was standardized to the RMP value determined immediately after break-in (DHC  $V_{1/2} = -109 \pm 2.0$  mV,  $k = 9.2 \pm 0.7$  mV,  $n = 7$ ; VHC  $V_{1/2} = -93 \pm 0.6$  mV,  $k = 9.5 \pm 0.6$  mV,  $n = 3$ ;  $V_{1/2}$  Wilcoxon's rank sum test,  $P < 0.05$ ;  $k$  Wilcoxon's rank sum test,  $P > 0.05$ ).

We next investigated whether this difference in the voltage range of activation was accompanied by a difference in the kinetic properties of  $I_h$ . The time course of  $I_h$  activation was described assuming double-exponential decay (Fig. 4A), and fast ( $\tau_{fast}$ ) and slow ( $\tau_{slow}$ ) time constants were determined over a range of membrane potentials (-90 to -30 mV,  $\Delta$  10 mV, relative to RMP; Fig. 4B).  $\tau_{fast}$ ,  $\tau_{slow}$ , and their respective fractional amplitudes (Frac $A_{fast}$  and Frac $A_{slow}$ ) showed similar trends across the range of investigated membrane potentials (Fig. 4, *B* and *C*). However, their absolute values were slightly offset by the difference in RMP between DHC and VHC neurons. The voltage dependence of  $\tau_{fast}$  ( $z_{fast}$ ) was similar for DHC and VHC patches [DHC  $z_{fast} = -1.1 \pm 0.1 e_0$  ( $n = 3$ ),

Table 2. Biophysical properties of  $I_h$  from DHC and VHC neurons

	ssG-V $V_{1/2}$ , mV	ssG-V Slope Factor, mV	tailG-V $V_{1/2}$ , mV	tailG-V Slope Factor, mV	Maximum $G$ Density, pS/ $\mu$ m <sup>2</sup>
DHC soma	-113.1 $\pm$ 4.7 (3)	8.2 $\pm$ 1.1 (3)	-109.5	8.9	2.3 $\pm$ 0.2 (3)
DHC pSR	-114.7 $\pm$ 2.4 <sup>a</sup> (3)	8.7 $\pm$ 1.1 <sup>c</sup> (3)	-107.3	10.7	3.3 $\pm$ 0.5 (3)
DHC dSR	-115.3 $\pm$ 1.1 <sup>b</sup> (12)	9.0 $\pm$ 0.5 (12)	-110.3	10.6	6.0 $\pm$ 0.8 (12)
VHC soma	-114.0 $\pm$ 1.6 (7)	9.3 $\pm$ 0.7 (7)	-109.2	12.4	3.2 $\pm$ 1.0 (7)
VHC pSR	-105.0 $\pm$ 1.5 <sup>a</sup> (5)	11.2 $\pm$ 0.2 <sup>c</sup> (5)	-110.5	10.1	3.4 $\pm$ 0.4 (4)
VHC dSR	-96.7 $\pm$ 1.6 <sup>b</sup> (7)	8.8 $\pm$ 0.4 (7)	-104.9	7.6	8.9 $\pm$ 2.1 (6)
			-105.1 $\pm$ 1.3 (4)	12.2 $\pm$ 0.9 (4)	
			-95.0 $\pm$ 2.0 <sup>d</sup> (7)	8.0 $\pm$ 0.7 (7)	

Values are means  $\pm$  SE. Measurements with  $n$  values < 3 are listed individually and were not subjected to statistical analysis. Otherwise,  $n$  values are indicated in parentheses. Membrane potential of 1/2 maximal conductance ( $V_{1/2}$ ) and slope factor of the conductance-voltage ( $G$ - $V$ ) relationships (ssG-V and tailG-V) and maximal  $G$  density of  $I_h$  recorded from soma (0  $\mu$ m), proximal stratum radiatum (pSR, 100–200  $\mu$ m), and distal stratum radiatum (dSR, 200–300  $\mu$ m) from DHC and VHC neurons were tabulated. Statistical significance was determined with either a Student's *t*-test or the Wilcoxon rank sum test with  $P < 0.05$  (see MATERIALS AND METHODS). Paired superscripted letters indicate significant differences between DHC neurons and VHC neurons.

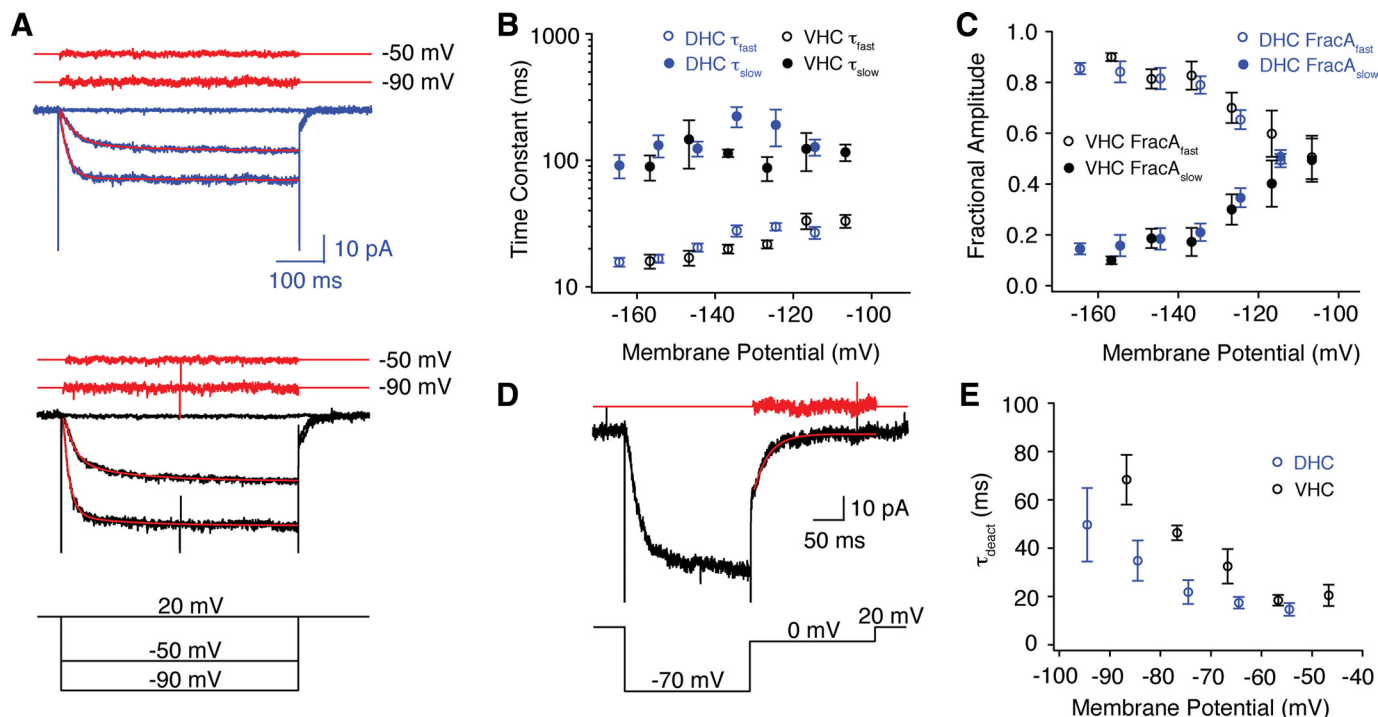


Fig. 4. Voltage-dependent kinetics of  $h$ -channels from DHC and VHC neurons. *A*: the time course of activation was described assuming a double-exponential function for DHC (blue, *top*) and VHC (black, *bottom*) neurons. Fitted curves are displayed superimposed on the current traces (red lines), and residuals (*top*) are plotted separately for the indicated step hyperpolarizations. Example fits are from the traces displayed in Fig. 3*A*, and all kinetic measurements were made from dendritic recordings 200–300  $\mu\text{m}$  from to soma. *B* and *C*: both fast and slow time constants describing activation ( $\tau$ ; *B*) were qualitatively similar across a range of membrane potentials for  $I_h$  measured from DHC and VHC neurons, as were their fractional amplitudes (FracA; *C*). *D*: tail currents were elicited by step depolarizations ranging from  $-20$  to  $20$  mV (relative to RMP) and in  $10$ -mV increments after a  $200$ -ms step hyperpolarization to  $-70$  mV (relative to RMP). Tail currents were described assuming an exponential function (fitted red curve), with the residual plotted separately (red trace, *top*). *E*: the time constant of deactivation ( $\tau_{\text{deact}}$ ) for  $I_h$  from DHC and VHC plotted across a range of membrane potentials.

VHC  $z_{\text{fast}} = -1.0 \pm 0.2 e_0$  ( $n = 3$ ); Wilcoxon's rank sum test,  $P > 0.05$ ], whereas the voltage dependence of  $\tau_{\text{slow}}$  ( $z_{\text{slow}}$ ) was not determined because of the high variability in this time constant. However, from casual inspection it seems as though  $\tau_{\text{slow}}$  is nearly voltage independent in VHC dendrites but may be weakly voltage dependent in DHC dendrites (see below). Tail currents were elicited from step depolarizations to membrane potentials ranging from  $-20$  to  $20$  mV (relative to RMP) after a maximally activating  $200$ -ms step hyperpolarization to  $-70$  mV (Fig. 4*D*). The time course of the tail current was described assuming exponential decay (sometimes following a slight delay; Fig. 4*D*), and the resulting time constant  $\tau_{\text{deact}}$  was plotted across a range of membrane potentials ( $-20$  to  $20$  mV,  $\Delta 10$  mV, relative to RMP; Fig. 4*E*). The voltage dependence of  $\tau_{\text{deact}}$  ( $z_{\text{deact}}$ ) was significantly larger for VHC neurons than DHC neurons [DHC  $z_{\text{deact}} = 1.2 \pm 0.2 e_0$  ( $n = 5$ ), VHC  $z_{\text{deact}} = 2.4 \pm 0.2 e_0$  ( $n = 4$ ); Wilcoxon's rank sum test,  $P < 0.05$ ]. The sum of the absolute values for  $z_{\text{fast}}$  and  $z_{\text{deact}}$  ( $z_{\text{sum}}$ ) closely approximates the voltage dependence of the tail  $G$ - $V$  curve determined from the slope factor ( $z_{\text{total}}$ ) for VHC ( $z_{\text{sum}} = 3.4 e_0$ ,  $z_{\text{total}} = 3.5 \pm 0.4 e_0$ ) but not DHC ( $z_{\text{sum}} = 2.4 e_0$ ,  $z_{\text{total}} = 2.9 \pm 0.2 e_0$ ) dendrites. This discrepancy likely reflects the undetermined voltage dependence of  $\tau_{\text{slow}}$  for  $I_h$  from DHC dendrites.

Given this significant difference in the voltage range of activation for  $h$ -channels from DHC and VHC dendrites in dSR, we investigated the functional properties of  $h$ -channels along the remaining accessible somatodendritic axis.  $I_h$  measurements along this axis were binned into three groups: soma,

pSR, and dSR. Unfortunately, somatic  $I_h$  was too small to reliably determine the  $G$ - $V$  relationship from the peak of the tail current because of the low  $h$ -conductance density at this location (peak tail current amplitudes were often  $< 2$  pA; Fig. 5*F*, Table 2). We therefore determined the  $G$ - $V$  relationship based on the steady-state current responses to each voltage step, and refer to this as the steady-state  $G$ - $V$  relationship (ss $G$ - $V$ ). The reversal potentials of  $I_h$  ( $E_h$ ) from DHC and VHC neurons were experimentally determined from dendritic recordings in dSR [DHC  $E_h = -5.1 \pm 4.6$  mV ( $n = 6$ ), VHC  $E_h = -4.9 \pm 3.8$  mV ( $n = 5$ ); data not shown]. ss $G$ - $V$  relationships were indistinguishable from tail $G$ - $V$  relationships measured from the same dendritic patches for both DHC and VHC neurons and were thereafter used to compare the  $G$ - $V$  relationships of  $h$ -channels across the somatodendritic axis (data not shown). ss $G$ - $V$  relationships measured from the soma of DHC and VHC neurons were indistinguishable (Fig. 5, *A*, *D*, and *E*). However, the ss $G$ - $V$  relationship shifted to more depolarized membrane potentials as the recording location moved progressively farther from the soma for VHC neurons but not DHC neurons (Fig. 5, *A*–*D*). This shift was due to a change in the  $V_{1/2}$  of the ss $G$ - $V$  relationship that occurred within the first  $100 \mu\text{m}$  of the apical dendrite for VHC neurons and continued to depolarize as the recording location moved toward the dSR ( $V_{1/2\text{dSR}} - V_{1/2\text{soma}} = 17$  mV; Fig. 5, *A*–*D*, Table 2). The voltage dependence of the ss $G$ - $V$  relationship (measured as the slope factor,  $k$ ), however, did not change along the somatodendritic axis, although  $k$  was significantly larger for VHC than DHC neurons in pSR (Fig.

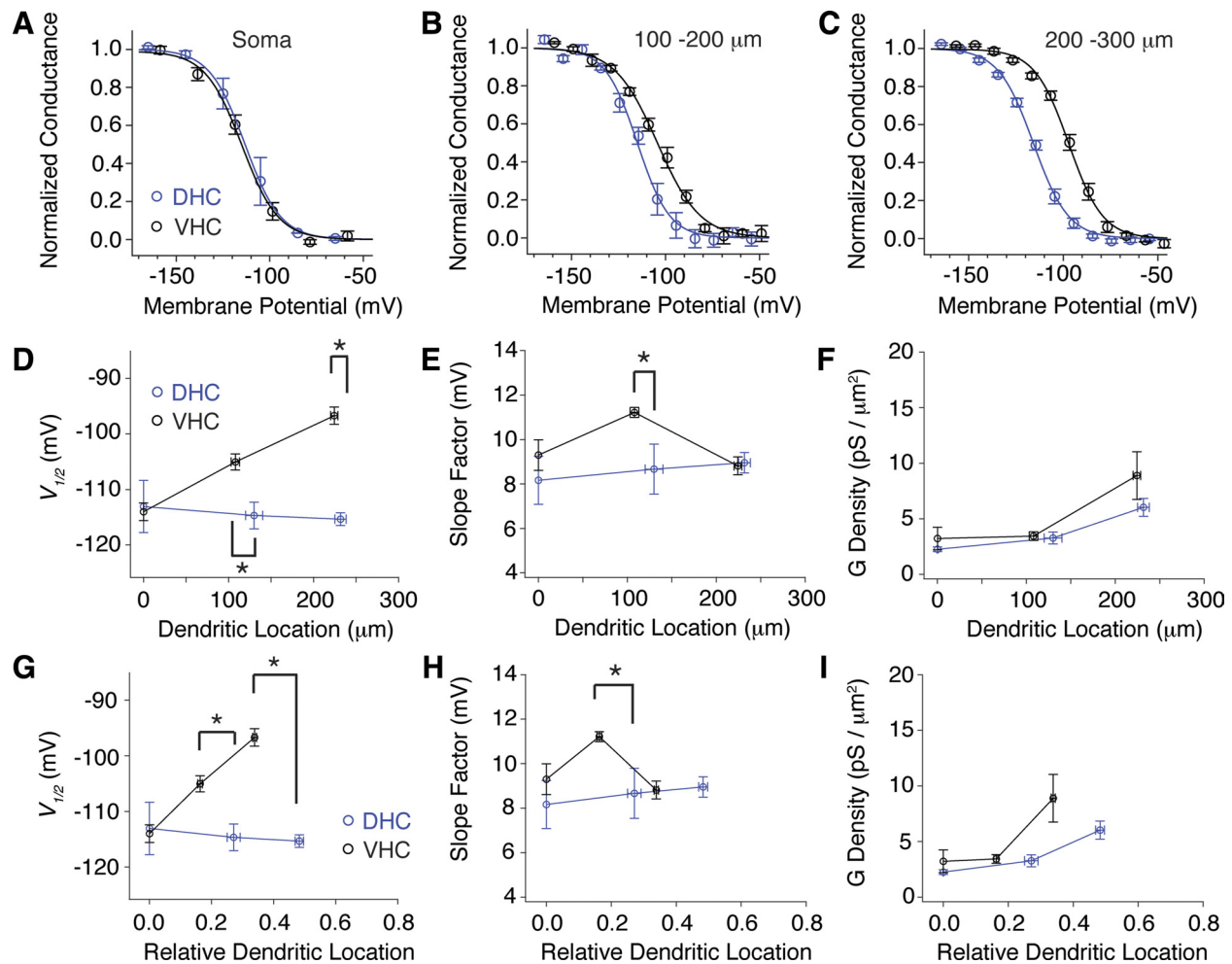


Fig. 5. Somatodendritic gradients of the functional properties of *h*-channels from DHC and VHC neurons. *A–C*: voltage dependence of activation for *h*-channels from somatic (0  $\mu\text{m}$ ; *A*), proximal stratum radiatum (pSR, 100–200  $\mu\text{m}$ ; *B*), and distal stratum radiatum (dSR, 200–300  $\mu\text{m}$ ; *C*) patches from DHC and VHC neurons were described assuming a Boltzmann function with the following fit parameters: soma: DHC  $V_{1/2} = -113$  mV,  $k = 9.5$  mV, VHC  $V_{1/2} = -115$  mV,  $k = 8.8$  mV; pSR: DHC  $V_{1/2} = -115$  mV,  $k = 8.5$  mV, VHC  $V_{1/2} = -104$  mV,  $k = 11.3$  mV; dSR: DHC  $V_{1/2} = -116$  mV,  $k = 9.3$  mV, VHC  $V_{1/2} = -97$  mV,  $k = 9.0$  mV. All conductance values for this figure were determined from the maximal current at each membrane potential. *D*:  $V_{1/2}$  was significantly more depolarized for VHC neurons than DHC neurons in pSR (Wilcoxon rank sum test,  $*P < 0.05$ ) and dSR (Student's *t*-test,  $*P < 0.05$ ) but not the soma (Wilcoxon rank sum test,  $P > 0.05$ ). *E*: slope factor ( $k$ ) was significantly larger for VHC neurons than DHC neurons in pSR (Wilcoxon rank sum test,  $*P < 0.05$ ) but not the soma (Wilcoxon rank sum test,  $P > 0.05$ ) or dSR (Student's *t*-test,  $P > 0.05$ ). *F*: conductance density was not significantly different between VHC and DHC neurons at the soma (Wilcoxon rank sum test,  $P > 0.05$ ), pSR (Wilcoxon rank sum test,  $P > 0.05$ ), or dSR (Wilcoxon rank sum test,  $P > 0.05$ ). *G–I*: the  $V_{1/2}$  value (*G*), the slope factor (*H*), and the maximal conductance density (*I*) were replotted on a normalized somatodendritic axis that accounts for the different lengths of the apical dendrites of DHC and VHC neurons. *n* Values are listed in Table 2.

5E, Table 2). The physiological significance of this latter observation, however, is not clear. The *G* density increased similarly for both DHC and VHC neurons with increasing distance from the soma (Fig. 5*F*, Table 2). These trends were also apparent when the  $V_{1/2}$ ,  $k$ , and *G* density were displayed on a normalized scale that accounts for differences in the overall lengths of DHC and VHC apical dendrites (Fig. 5, *G–I*; Dougherty et al. 2012). Together, these observations highlight profound distance-dependent differences in voltage-dependent *h*-channel gating between DHC and VHC neurons.

**Somatodendritic expression of HCN1 and HCN2 along dorsal-ventral axis of CA1 pyramidal neurons.** The cell-attached patch-clamp experiments indicate that differences in voltage-dependent gating of *h*-channels, rather than number, strongly influence the dorsal-ventral differences in *h*-channel function detected with whole cell patch-clamp recordings. One possible

substrate for such differences is a shift in the relative abundance of the two *h*-channel subunits present in CA1 pyramidal neurons, HCN1 and HCN2, which differ in their voltage-dependent properties when expressed as homotetramers (Chen et al. 2001; Robinson and Siegelbaum 2003; Ulens and Tytgat 2001). Specifically, the voltage range of activation for HCN2 homotetramers is significantly more hyperpolarized than that for HCN1 homotetramers. The differential voltage range of *h*-channel gating we describe in VHC and DHC neurons, then, may be driven by differential expression levels of these two subunits.

As an initial estimate of HCN subunit protein levels in CA1, we performed Western blot analyses for HCN1 and HCN2 in microdissected slices of dorsal and ventral CA1 (Fig. 6*A*). These analyses indicated that homogenized, microdissected slices of CA1 from VHC had more total HCN1 and HCN2 protein than slices from DHC [Fig. 6*A*; main effect of dorsal/

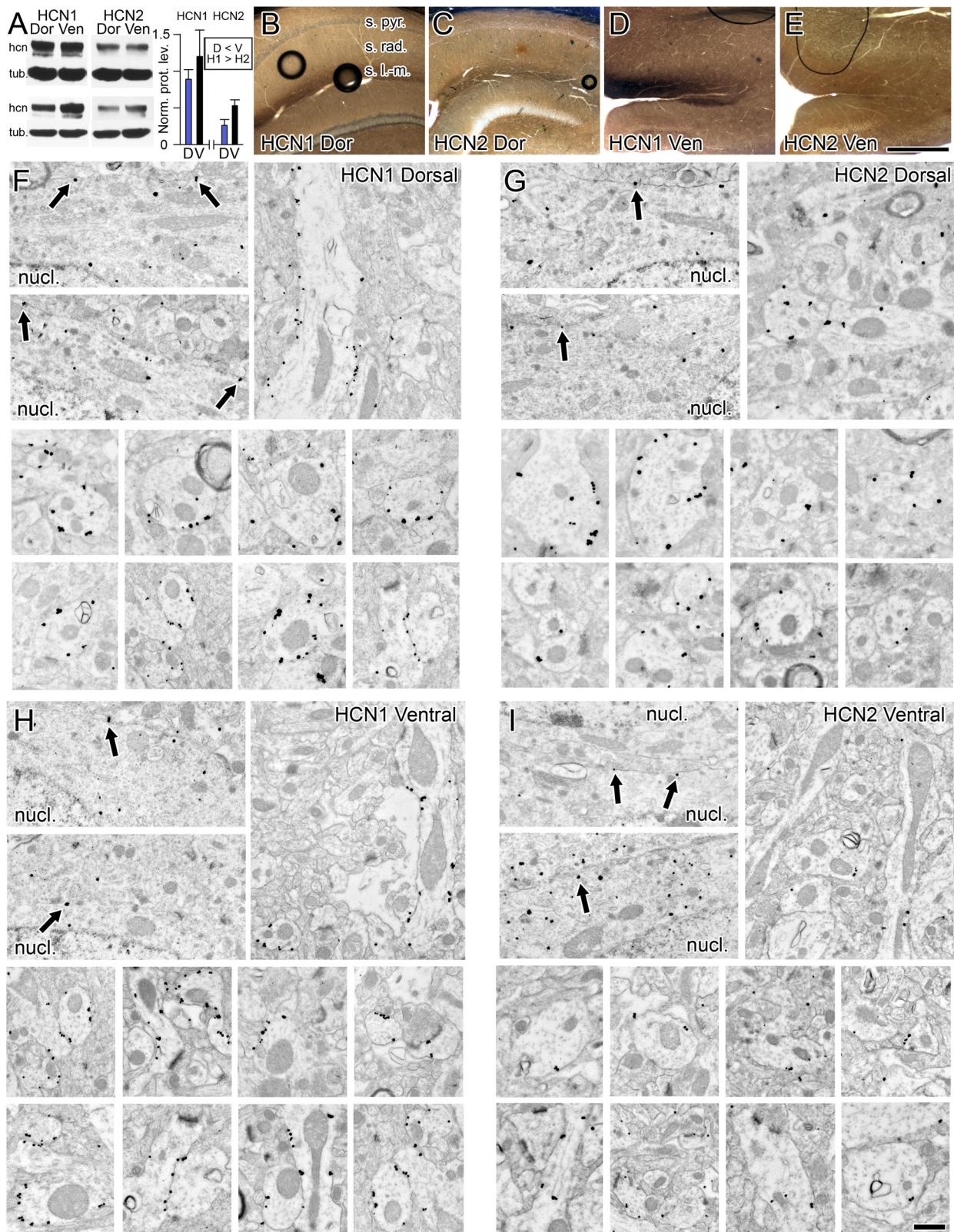


Fig. 6. Expression of HCN1 and HCN2 in dorsal and ventral CA1. *A*: HCN1, HCN2, and  $\alpha$ -tubulin (tub) protein levels in microdissected slices of dorsal and ventral CA1 from 2 representative rats. Error bars represent SE. *B–E*: dorsal (*B* and *C*) and ventral (*D* and *E*) hippocampal slices immunostained for HCN1 (*B* and *D*) or HCN2 (*C* and *E*) with the preembedding silver-intensified ultrasmall immunogold electron microscopy technique. The darkened appearance of tissue in SLM is due to the presence of silver-intensified immunogold particles. s. pyr., CA1 stratum pyramidale; s. rad., CA1 stratum radiatum; s.l.-m., CA1 stratum lacunosum-moleculare. Scale bar, 500  $\mu$ m. *F–I*: electron micrographs of hippocampal CA1 from dorsal (*F* and *G*) and ventral (*H* and *I*) hippocampus immunostained for HCN1 (*F* and *H*) or HCN2 (*G* and *I*). *F–I*, top left: electron micrographs of CA1 pyramidal neuron somata (arrows denote membrane-bound particles; nucl., nucleolus). Remaining subpanels are electron micrographs of immunopositive dendrites in SLM from each corresponding region. Scale bar in *I*, 1  $\mu$ m and 0.5  $\mu$ m for somata and dendrite subpanels, respectively.

ventral:  $F_{(1,16)} = 6.15$ ,  $P < 0.05$ ]. Furthermore, overall protein levels for HCN1 were higher than those for HCN2, regardless of whether slices were taken from the DHC or the VHC [ $P < 0.05$ ; main effect of HCN1/HCN2:  $F_{(1,16)} = 30.85$ ,  $P < 0.01$ ]. Such analyses, however, lack the resolution required for quantitative comparison of HCN subunit expression, particularly for segregating membrane-bound from cytoplasmic HCN channels. To more accurately determine whether changes in HCN subunit distribution contribute to the biophysical differences between dorsal and ventral CA1 pyramidal neurons, we analyzed HCN1 and HCN2 expression with serial section silver-intensified immunogold EM of CA1 pyramidal neuron somata, their proximal dendrites, and their distal dendrites.

Like peroxidase-based EM techniques, light microscopy of the silver-intensified immunogold tissue provides an initial estimate of protein expression and localization. Unlike peroxidase-based techniques, however, the darkened reaction product in tissue processed with the silver-intensified immunogold protocol is due to individual, nondiffusible, silver-intensified immunogold particles (e.g., Lörincz et al. 2002; Notomi and Shigemoto 2004). Such particulate markers enable the immunolocalization of proteins with ultrastructural resolution and permit quantitative comparisons via estimates of particle densities per unit dendritic surface area.

At the light microscopic level, both HCN1 and HCN2 expression showed distal enrichment in CA1, with intense bands of immunoreactivity in the SLM (Fig. 6, B–E), although the band within SLM appeared least intense for HCN2 in ventral CA1. Ultrastructural immunolocalization verified such observations, as silver-intensified immunogold particles for both HCN1 and HCN2 were projected onto the dendritic membrane in a ringlike manner in dorsal and ventral CA1 slices, with an abrupt increase in immunoreactivity in the distal dendrites of SLM (Fig. 6, F–I). Again, the distal enrichment was least apparent in ventral slices immunostained for HCN2 (Fig. 6J). Within the stratum pyramidale, clusters of immunogold particles for HCN1 and HCN2 were also projected onto the membrane of CA1 pyramidal neuron somata and scattered throughout their cytoplasm (Fig. 6, F–I).

Three-dimensional reconstructions of dendrites and their spines indicated that most of the immunogold particles for both HCN1 and HCN2 were projected onto the dendritic membrane (HCN1 dorsal  $70.0 \pm 1.4\%$ , HCN1 ventral  $75.0 \pm 0.9\%$ ; HCN2 dorsal  $69.9 \pm 1.5\%$ , HCN2 ventral  $64.0 \pm 1.2\%$ ). The remaining particles were primarily within the dendritic cytoplasm, although particles were occasionally found projected onto the membrane of dendritic spines (Fig. 7A). Compared with immunolabeled dendrites, immunolabeled spines were rare and so were excluded from the analyses. MANCOVA of 1,032 dendrites using dendritic diameter as the covariate revealed that, overall, SLM dendrites were more immunoreactive for HCN1 and HCN2 than pSR dendrites, and thus both HCN subunits exhibit distal enrichment in dorsal and ventral CA1 [Fig. 7, B and C; HCN1 main effect of proximal/distal:  $F_{(1,447)} = 83.62$ ,  $P < 0.001$ ; HCN2 main effect of proximal/distal:  $F_{(1,573)} = 98.50$ ,  $P < 0.001$ ; see also Table 3].

This general pattern, however, exhibited functionally interesting variations in a compartment- and subunit-specific manner. For example, comparison of HCN2 expression showed a main effect of dorsal/ventral [ $F_{(1,573)} = 64.60$ ,  $P < 0.001$ ; Fig. 7, B and C], driven by the overall lower levels of HCN2

expression in ventral CA1 dendrites. Additionally, HCN subunit immunoreactivity among CA1 pyramidal neuron somata differed, with high somatic HCN1 expression in dorsal CA1 compared with HCN1 expression in ventral CA1 somata and HCN2 expression in both dorsal and ventral CA1 somata [ $F_{(1,24)} = 7.46$ ,  $P = 0.012$ ; Fig. 7C]. Remarkably, when the expression levels of both HCN subunits were considered together, the ratio of HCN1 to HCN2 immunoreactivity increased progressively with distance from the soma in ventral CA1 slices, whereas this ratio remained constant along this same axis in dorsal CA1 (Fig. 7C). Finally, underscoring the principal role of subunit specificity in HCN channel function among SLM dendrites, there were significantly more highly immunoreactive dendrites for HCN1 in ventral CA1 ( $\chi^2 = 22.23$ ,  $df = 8$ ,  $P < 0.01$ ; Fig. 7D) and significantly more weakly immunoreactive dendrites for HCN2 in ventral CA1 ( $\chi^2 = 48.53$ ,  $df = 4$ ,  $P < 0.0001$ ; Fig. 7D).

Taken together, the serial section preembedding ultrasmall immunogold electron microscopic analyses indicate that dendrites in ventral CA1 have more HCN1-containing and fewer HCN2-containing *h*-channels than dendrites in dorsal CA1. Moreover, the relative abundance of HCN1 increases progressively with distance from the soma in ventral CA1 but remains constant along the somatodendritic axis in dorsal CA1. The patch-clamp physiology and EM experiments are therefore in remarkable agreement with the notion that dorsal-ventral differences in *h*-channel gating are attributable to the proportion of HCN1 on the plasma membrane increasing progressively with distance from the soma in VHC neurons but not DHC neurons.

## DISCUSSION

In this study, we report significant differences in the functional properties of  $I_h$  and the expression of HCN1 and HCN2 channel subunits for CA1 pyramidal neurons across the dorsal-ventral hippocampal axis. Current-clamp experiments suggest that  $I_h$  is larger in VHC neurons than DHC neurons, and direct measurements of  $I_h$  from cell-attached voltage-clamp experiments indicate that the somatodendritic *h*-conductance gradient was functionally augmented by a depolarizing shift in the  $V_{1/2}$  of *h*-channels from VHC, but not DHC, neurons. Serial section immunogold EM experiments demonstrate that the expression levels of HCN1 and HCN2 subunits differ significantly across the dorsal-ventral axis, such that the HCN1-to-HCN2 ratio matches the distance-dependent profiles of the  $V_{1/2}$  for *h*-channels along the somatodendritic axes of DHC and VHC neurons. This latter observation likely underlies the functionally augmented *h*-conductance gradient that contributes to the significantly depolarized RMP of VHC neurons.

*VHC neurons exhibit an augmented h-conductance gradient.* The  $I_h$ -related differences in RMP described above likely stem from *h*-channels that exhibit different functional properties in DHC and VHC neurons. Interestingly, differences in the functional properties of *h*-channels were observed across both the dorsal-ventral hippocampal and somatodendritic axes and demonstrate the existence of two distinct somatodendritic  $I_h$  gradients: 1) a DHC-type gradient in which the *h*-conductance density increases with distance from the soma but the  $V_{1/2}$  of voltage-dependent *h*-channel gating is constant and 2) a VHC-type gradient in which both the *h*-conductance density in-

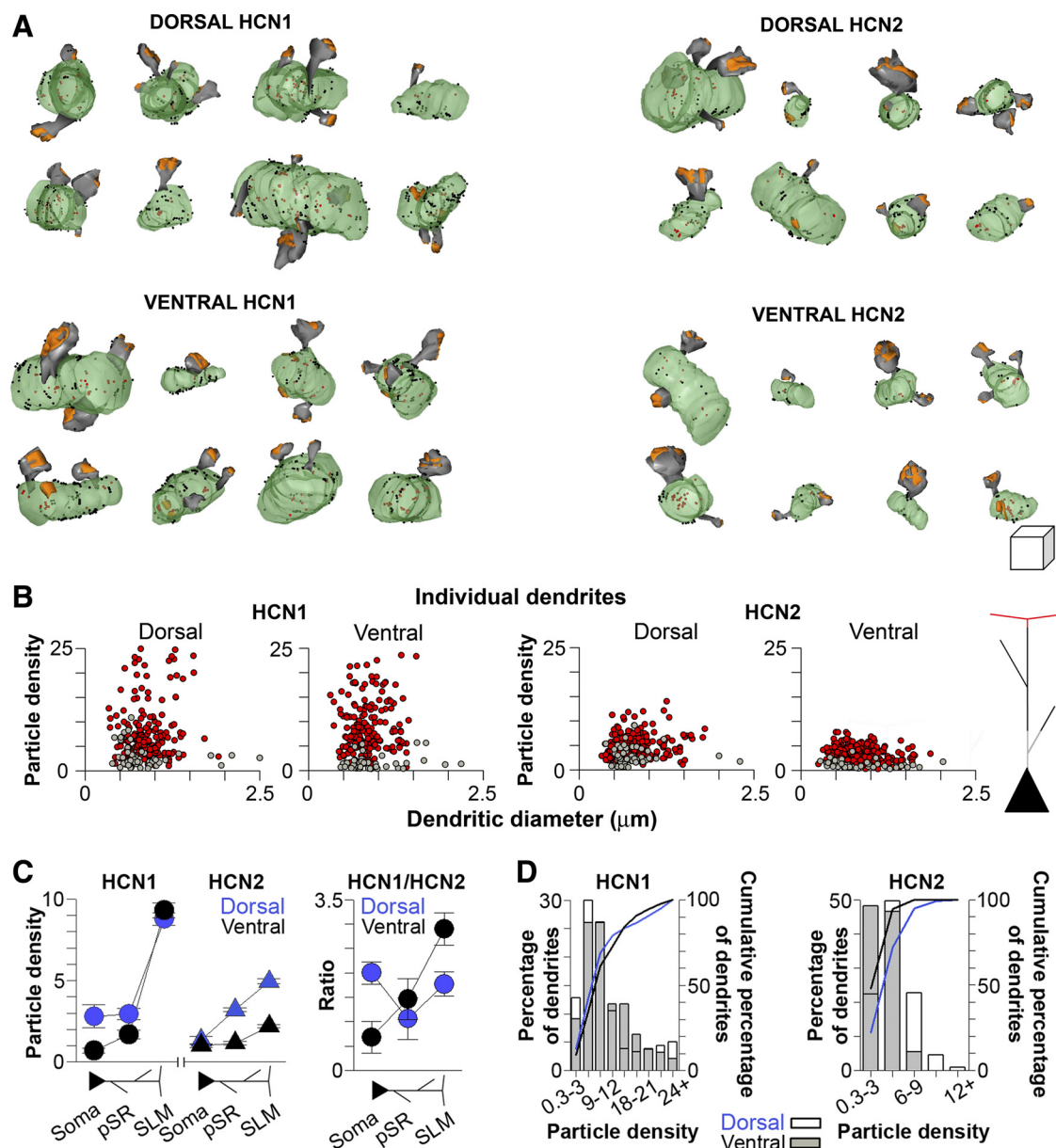


Fig. 7. Subunit-specific differences in HCN channel expression in dorsal and ventral CA1. *A*: 3-dimensional reconstructions from serial sections through dendrites immunopositive for HCN1 (left) or HCN2 (right) from dorsal (top) and ventral (bottom) CA1. Cube =  $1 \mu\text{m}^3$ . Green, dendrite; gray, spines; orange, postsynaptic density; black circles, membrane-bound immunogold particles; red circles, cytoplasmic immunogold particles. *B*: scatterplots of particle density as a function of dendritic diameter (HCN1, left; HCN2, right) for individual dendrites in pSR (gray) and SLM (red) of dorsal and ventral CA1. *C*, left: particle densities for HCN1 (left)- or HCN2 (right)-immunopositive somata and dendrites in pSR and SLM of dorsal and ventral hippocampal region CA1. Right: ratio of HCN1 to HCN2 particle densities at the soma and in pSR or SLM dendrites in dorsal and ventral CA1. *D*: histograms of % and cumulative % of dendrites in dorsal (blue lines; open bars) and ventral (black lines; gray bars) CA1 SLM harboring a given number of membrane-bound immunogold particles for HCN1 (left) or HCN2 (right).

creases and the  $V_{1/2}$  of voltage-dependent  $h$ -channel gating depolarizes with distance from the soma. The VHC-type gradient can be considered an augmented  $h$ -conductance gradient, as the underlying gradient of  $h$ -conductance density is functionally augmented by the distance-dependent depolarization of the  $V_{1/2}$  of voltage-dependent  $h$ -channel gating (e.g., more  $h$ -conductance is present within the neuron's range of subthreshold membrane potentials because of the depolarizing shift in  $V_{1/2}$ ). Although distance-dependent changes in the  $V_{1/2}$  of  $I_h$  have been described previously (Angelo et al. 2007; Berger et al. 2001; Bullis et al. 2007; Kole et al. 2006; Magee 1998), this aspect of the  $h$ -conductance gradient has received

relatively little attention with regard to the integrative properties of dendrites. Future experiments will be directed toward understanding the respective roles that DHC-type and VHC-type  $h$ -conductance gradients play in dendritic integration for CA1 pyramidal neurons.

*Potential mechanisms.* Our study provides a relatively straightforward molecular mechanism for the functionally augmented  $h$ -conductance gradient observed in VHC neurons. Specifically, we propose that the functional augmentation of the  $h$ -conductance gradient is driven by a distance-dependent increase in the HCN1-to-HCN2 ratio along the somatodendritic axis of VHC neurons (Fig. 7C). Experimental results from

Table 3. HCN subunit immunoexpression levels as a function of neuronal compartment and hippocampal region for CA1 pyramidal neurons

Region	HCN Subunit	Compartment	<i>n</i>	Total Membrane Surface Area, $\mu\text{m}^2$	Membrane-Bound Particle Density ( $\pm\text{SE}$ )	Cytoplasmic Particle Density ( $\pm\text{SE}$ )	% Membrane Bound
Dorsal CA1	HCN1	Soma	6	33.21	2.80 ( $\pm 0.69$ )	8.73 ( $\pm 1.21$ )	24
		Prox. Den.	46	106.62	2.95 ( $\pm 0.34$ )	2.32 ( $\pm 0.28$ )	57
		Dist. Den.	180	621.36	8.77 ( $\pm 0.52$ )	3.17 ( $\pm 0.18$ )	70
Ventral CA1	HCN1	Soma	5	22.75	0.70 ( $\pm 0.15$ )	9.19 ( $\pm 1.32$ )	7
		Prox. Den.	40	110.11	1.69 ( $\pm 0.24$ )	1.05 ( $\pm 0.18$ )	62
		Dist. Den.	188	502.83	9.31 ( $\pm 0.46$ )	3.07 ( $\pm 0.18$ )	75
Dorsal CA1	HCN2	Soma	9	44.14	1.34 ( $\pm 0.25$ )	10.46 ( $\pm 1.60$ )	12
		Prox. Den.	52	115.13	2.82 ( $\pm 0.24$ )	2.93 ( $\pm 0.31$ )	53
		Dist. Den.	224	584.01	4.94 ( $\pm 0.15$ )	2.89 ( $\pm 0.18$ )	70
Ventral CA1	HCN2	Soma	8	40.07	1.01 ( $\pm 0.12$ )	11.34 ( $\pm 1.89$ )	9
		Prox. Den.	42	90.15	1.16 ( $\pm 0.11$ )	1.45 ( $\pm 0.19$ )	51
		Dist. Den.	260	762.96	3.21 ( $\pm 0.10$ )	2.02 ( $\pm 0.10$ )	64

Values are HCN subunit immunoexpression levels (in the form of particle densities per  $\mu\text{m}^2$  of dendritic/somatic surface area) as a function of neuronal compartment and hippocampal axis in CA1 pyramidal neurons.

heterologous expression systems demonstrate that the  $V_{1/2}$  for homotetrameric HCN1 channels is significantly more depolarized than the  $V_{1/2}$  for homotetrameric HCN2 channels ( $\Delta V_{1/2} \approx 10\text{--}15$  mV, depending on experimental conditions) (Chen et al. 2001; Ulens and Tytgat 2001). Accordingly, heterotetrameric HCN1/HCN2 channels (the presumed subunit composition of native *h*-channels in CA1 pyramidal neurons) exhibit  $V_{1/2}$  values that lie between those of either homotetrameric HCN1 or HCN2 channels, with an increased HCN1-to-HCN2 ratio favoring a more depolarized  $V_{1/2}$  value (Chen et al. 2001; Ulens and Tytgat 2001). Therefore, differences in the ratio of HCN1 to HCN2 expression levels represent a plausible candidate mechanism for the functional augmentation of the *h*-conductance gradient (assuming that differences in subunit expression translate into differences in *h*-channel subunit composition). However, the influence of secondary factors such as interaction with  $\beta$ -subunits (such as TRIP8b), posttranslational modification (i.e., calcineurin and p38 MAPK), and interaction with chemical ligands (cAMP and PIP<sub>2</sub>) cannot be ruled out on the basis of our data (Chen et al. 2001; Jung et al. 2010; Lewis et al. 2009; Pian et al. 2006; Poolos et al. 2006; Santoro et al. 2009; Ulens and Tytgat 2001; Zolles et al. 2006, 2009).

Although the shifting HCN1-to-HCN2 subunit ratio is consistent with changes in the  $V_{1/2}$  values of  $I_h$  along the somatodendritic axis, the total particle densities (HCN1 + HCN2) for each hippocampal region suggest that the maximal *h*-conductance density should be greater in DHC than VHC neurons (Fig. 7C). We did not detect, however, any significant difference in the maximal *h*-conductance density between DHC and VHC neurons at any somatodendritic recording location (Fig. 5F). This discrepancy may result from technical limitations of estimating patch surface area or, alternatively, could stem from the expression of functionally impaired (or nonfunctional) *h*-channels in DHC neurons. The latter argument has been used to account for a similar discrepancy between immunohistochemical and functional (cell-attached voltage-clamp) measurements of  $I_h$ /HCN channel density in SLM, and between estimates of the density of voltage-gated sodium channels expressed at the axon initial segment (Bittner et al. 2012; Kole and Stuart 2012).

**Physiological significance.** CA1 pyramidal neurons and layer II stellate neurons of the MEC both exhibit location-

dependent firing fields that become progressively larger along their respective dorsal-ventral axes (Hafting et al. 2005; Jung et al. 1994). These two cell types also share a gradient in somatic  $R_{in}$ , such that the somatic  $R_{in}$  increases along their respective dorsal-ventral axes (Dougherty et al. 2012; Garden et al. 2008). Although  $I_h$  influences the  $R_{in}$  and shapes both place and grid fields, the intercellular  $I_h$  gradients show opposing trends across the dorsal-ventral hippocampal and MEC axes (Giocomo et al. 2011; Hussaini et al. 2011; Robinson and Siegelbaum 2003). Specifically,  $I_h$  increases across the dorsal-ventral hippocampal axis for CA1 pyramidal neurons but decreases along the dorsal-ventral axis of the MEC for layer II stellate neurons (Garden et al. 2008). This leads to a significant depolarization of the RMP across the dorsal-ventral hippocampal axis, whereas such a gradient in RMP is not seen in layer II stellate neurons of the MEC (Garden et al. 2008). This latter observation is likely due to a second intercellular gradient of a potassium leak conductance that offsets the depolarizing influence of  $I_h$  on RMP in the MEC (Garden et al. 2008). The relationship between RMP and the voltage dependence of *h*-channel gating for CA1 pyramidal neurons, however, has some interesting physiological ramifications, especially with regard to  $f_R$ . Despite significant differences in  $f_R$  (at  $-73$  mV), no significant differences in  $f_R$  (at RMP) were detected between DHC and VHC neurons (Fig. 2F). It appears, then, that the differences in RMP and the voltage-dependent gating properties of *h*-channels “balance out” and lead to a situation in which DHC and VHC neurons exhibit similar  $I_h$ -related electrophysiological properties, but at significantly different RMPs. This could lead to profound differences in dendritic integration between DHC and VHC neurons.

**Relationship to previous studies.** In a recent study, Marcelin et al. investigated the  $I_h$ -related properties and expression of HCN channel subunits in the distal dendrites of adult rats and observed a greater amplitude of  $I_h$  (using whole cell voltage-clamp) and higher  $f_R$  for VHC neurons than DHC neurons (Marcelin et al. 2012). Furthermore, as we found (Fig. 6A), these authors observed that both HCN1 and HCN2 channel subunit expression were greater in the VHC than the DHC by Western blot analyses (of whole hippocampal homogenates; Marcelin et al. 2012). In light of the results of the Western blot analyses in the present study and those by Marcelin et al.

(2012), one would reasonably conclude that the overall HCN channel subunit expression is greater in the VHC than the DHC. The ultrastructural immunolocalization of HCN1 and HCN2 with immunogold EM, however, clearly shows that CA1 pyramidal neurons from VHC neurons actually express less HCN2 than DHC neurons (Fig. 7C). This observation is in remarkable agreement with the functional properties of  $I_h$  from cell-attached voltage-clamp recordings (Figs. 3 and 5) and highlights the power of our multidisciplinary experimental approach.

**Summary.** In summary, our results indicate that VHC neurons have greater functional  $I_h$  than DHC neurons. Cell-attached voltage-clamp recordings of  $I_h$  along the somatodendritic axis revealed a functional augmentation of the  $I_h$  gradient due to a distance-dependent shift in the voltage-dependent properties of  $h$ -channels for VHC neurons but not DHC neurons. Serial section immunogold EM labeling of HCN1 and HCN2 revealed distinct somatodendritic expression profiles for DHC and VHC neurons that closely matched our functional observations. Together, these results demonstrate clear dorsal-ventral differences in the functional properties and subunit expression profiles of a voltage-gated ion channel that serves as a key regulator of the intrinsic electrophysiological properties of CA1 pyramidal neurons.

#### ACKNOWLEDGMENTS

We thank Drs. Darrin Brager and Brian Kalmbach for critically evaluating this manuscript, as well as the entire Johnston and Nicholson laboratories for their constant input on this project.

#### GRANTS

This work was supported by National Institutes of Health Grants R01-MH-048432 (D. Johnston), F32-MH-090665 (K. A. Dougherty), R01-NS-59934 (D. M. Chetkovich), R00-AG-031574 (D. A. Nicholson), R01-AG-017139 (D. A. Nicholson), and T32-AG-000269 (E. W. Buss and K. M. Neuman) and the Charles and M. R. Shapiro Foundation (D. A. Nicholson).

#### DISCLOSURES

No conflicts of interest, financial or otherwise, are declared by the author(s).

#### AUTHOR CONTRIBUTIONS

Author contributions: K.A.D., D.A.N., L.M.D., D.M.C., and D.J. conception and design of research; K.A.D., D.A.N., E.W.B., and K.M.N. performed experiments; K.A.D., D.A.N., E.W.B., and K.M.N. analyzed data; K.A.D., D.A.N., E.W.B., and K.M.N. interpreted results of experiments; K.A.D., D.A.N., E.W.B., and K.M.N. prepared figures; K.A.D. and D.A.N. drafted manuscript; K.A.D., D.A.N., D.M.C., and D.J. edited and revised manuscript; K.A.D., D.A.N., and D.J. approved final version of manuscript.

#### REFERENCES

- Angelo K, London M, Christensen SR, Hausser M. Local and global effects of  $I_h$  distribution in dendrites of mammalian neurons. *J Neurosci* 27: 8643–8653, 2007.
- Bannerman DM, Rawlins JN, McHugh SB, Deacon RM, Yee BK, Bast T, Zhang WN, Pothuizen HH, Feldon J. Regional dissociations within the hippocampus—memory and anxiety. *Neurosci Biobehav Rev* 28: 273–283, 2004.
- Berger T, Larkum ME, Luscher HR. High  $I_h$  channel density in the distal apical dendrite of layer V pyramidal cells increases bidirectional attenuation of EPSPs. *J Neurophysiol* 85: 855–868, 2001.
- Bittner KC, Andrasfalvy BK, Magee JC. Ion channel gradients in the apical tuft region of CA1 pyramidal neurons. *PLoS One* 7: e46652, 2012.
- Brun VH, Solstad T, Kjelstrup KB, Fyhn M, Witter MP, Moser EI, Moser MB. Progressive increase in grid scale from dorsal to ventral medial entorhinal cortex. *Hippocampus* 18: 1200–1212, 2008.
- Bullis JB, Jones TD, Poolos NP. Reversed somatodendritic  $I_h$  gradient in a class of rat hippocampal neurons with pyramidal morphology. *J Physiol* 579: 431–443, 2007.
- Chen S, Wang J, Siegelbaum SA. Properties of hyperpolarization-activated pacemaker current defined by coassembly of HCN1 and HCN2 subunits and basal modulation by cyclic nucleotide. *J Gen Physiol* 117: 491–504, 2001.
- Dong HW, Swanson LW, Chen L, Fanselow MS, Toga AW. Genomic-anatomic evidence for distinct functional domains in hippocampal field CA1. *Proc Natl Acad Sci USA* 106: 11794–11799, 2009.
- Dougherty KA, Islam T, Johnston D. Intrinsic excitability of CA1 pyramidal neurons from the rat dorsal and ventral hippocampus. *J Physiol* 590: 5707–5722, 2012.
- Fanselow MS, Dong HW. Are the dorsal and ventral hippocampus functionally distinct structures? *Neuron* 65: 7–19, 2010.
- Fyhn M, Molden S, Witter MP, Moser EI, Moser MB. Spatial representation in the entorhinal cortex. *Science* 305: 1258–1264, 2004.
- Gage FH, Thompson RG. Differential distribution of norepinephrine and serotonin along the dorsal-ventral axis of the hippocampal formation. *Brain Res Bull* 5: 771–773, 1980.
- Garden DL, Dodson PD, O'Donnell C, White MD, Nolan MF. Tuning of synaptic integration in the medial entorhinal cortex to the organization of grid cell firing fields. *Neuron* 60: 875–889, 2008.
- Giocomo LM, Hasselmo ME. Knock-out of HCN1 subunit flattens dorsal-ventral frequency gradient of medial entorhinal neurons in adult mice. *J Neurosci* 29: 7625–7630, 2009.
- Giocomo LM, Hussaini SA, Zheng F, Kandel ER, Moser MB, Moser EI. Grid cells use HCN1 channels for spatial scaling. *Cell* 147: 1159–1170, 2011.
- Grigoryan G, Korkotian E, Segal M. Selective facilitation of LTP in the ventral hippocampus by calcium stores. *Hippocampus* 22: 1635–1644, 2012.
- Hafting T, Fyhn M, Molden S, Moser MB, Moser EI. Microstructure of a spatial map in the entorhinal cortex. *Nature* 436: 801–806, 2005.
- Hussaini SA, Kempadoo KA, Thuault SJ, Siegelbaum SA, Kandel ER. Increased size and stability of CA1 and CA3 place fields in HCN1 knockout mice. *Neuron* 72: 643–653, 2011.
- Jung MW, Wiener SI, McNaughton BL. Comparison of spatial firing characteristics of units in dorsal and ventral hippocampus of the rat. *J Neurosci* 14: 7347–7356, 1994.
- Jung S, Bullis JB, Lau IH, Jones TD, Warner LN, Poolos NP. Downregulation of dendritic HCN channel gating in epilepsy is mediated by altered phosphorylation signaling. *J Neurosci* 30: 6678–6688, 2010.
- Kole MH, Hallermann S, Stuart GJ. Single  $I_h$  channels in pyramidal neuron dendrites: properties, distribution, and impact on action potential output. *J Neurosci* 26: 1677–1687, 2006.
- Kole MH, Stuart GJ. Signal processing in the axon initial segment. *Neuron* 73: 235–247, 2012.
- Lewis AS, Schwartz E, Chan CS, Noam Y, Shin M, Wadman WJ, Surmeier DJ, Baram TZ, Macdonald RL, Chetkovich DM. Alternatively spliced isoforms of TRIP8b differentially control h channel trafficking and function. *J Neurosci* 29: 6250–6265, 2009.
- Lewis AS, Vaidya SP, Blais CA, Liu Z, Stoub TR, Brager DH, Chen X, Bender RA, Estep CM, Popov AB, Kang CE, Van Veldhoven PP, Bayliss DA, Nicholson DA, Powell CM, Johnston D, Chetkovich DM. Deletion of the hyperpolarization-activated cyclic nucleotide-gated channel auxiliary subunit TRIP8b impairs hippocampal  $I_h$  localization and function and promotes antidepressant behavior in mice. *J Neurosci* 31: 7424–7440, 2011.
- Lörincz A, Notomi T, Tamás G, Shigemoto R, Nusser Z. Polarized and compartment-dependent distribution of HCN1 in pyramidal cell dendrites. *Nat Neurosci* 5: 1185–1193, 2002.
- Magee JC. Dendritic hyperpolarization-activated currents modify the integrative properties of hippocampal CA1 pyramidal neurons. *J Neurosci* 18: 7613–7624, 1998.
- Magee JC. Dendritic  $I_h$  normalizes temporal summation in hippocampal CA1 neurons. *Nat Neurosci* 2: 508–514, 1999.
- Magee JC. Dendritic integration of excitatory synaptic input. *Nat Rev Neurosci* 1: 181–190, 2000.
- Maggio N, Segal M. Striking variations in corticosteroid modulation of long-term potentiation along the septotemporal axis of the hippocampus. *J Neurosci* 27: 5757–5765, 2007.
- Marcelin B, Lugo JN, Brewster AL, Liu Z, Lewis AS, McClelland S, Chetkovich DM, Baram TZ, Anderson AE, Becker A, Esclapez M, Bernard C. Differential dorso-ventral distributions of Kv4.2 and hyperpo-

- larization-activated cyclic adenosine monophosphate gated channel (HCN) proteins confer distinct integrative properties to hippocampal CA1 pyramidal cell distal dendrites. *J Biol Chem* 287: 17656–17661, 2012.
- Maurer AP, Vanrhoads SR, Sutherland GR, Lipa P, McNaughton BL.** Self-motion and the origin of differential spatial scaling along the septo-temporal axis of the hippocampus. *Hippocampus* 15: 841–852, 2005.
- Moser MB, Moser EI.** Functional differentiation in the hippocampus. *Hippocampus* 8: 608–619, 1998.
- Notomi T, Shigemoto R.** Immunohistochemical localization of  $I_h$  channel subunits, HCN1–4, in the rat brain. *J Comp Neurol* 471: 241–276, 2004.
- Pape HC.** Queer current and pacemaker: the hyperpolarization-activated cation current in neurons. *Annu Rev Physiol* 58: 299–327, 1996.
- Pian P, Bucchi A, Robinson RB, Siegelbaum SA.** Regulation of gating and rundown of HCN hyperpolarization-activated channels by exogenous and endogenous  $PIP_2$ . *J Gen Physiol* 128: 593–604, 2006.
- Poolos NP, Bullis JB, Roth MK.** Modulation of h-channels in hippocampal pyramidal neurons by p38 mitogen-activated protein kinase. *J Neurosci* 26: 7995–8003, 2006.
- Robinson RB, Siegelbaum SA.** Hyperpolarization-activated cation currents: from molecules to physiological function. *Annu Rev Physiol* 65: 453–480, 2003.
- Sakmann B, Neher E.** *Single-Channel Recording*. New York: Springer Science, 1995.
- Santoro B, Piskorowski RA, Pian P, Hu L, Liu H, Siegelbaum SA.** TRIP8b splice variants form a family of auxiliary subunits that regulate gating and trafficking of HCN channels in the brain. *Neuron* 62: 802–813, 2009.
- Ulens C, Tytgat J.** Functional heteromerization of HCN1 and HCN2 pacemaker channels. *J Biol Chem* 276: 6069–6072, 2001.
- van Groen T, Wyss JM.** Extrinsic projections from area CA1 of the rat hippocampus: olfactory, cortical, subcortical, and bilateral hippocampal formation projections. *J Comp Neurol* 302: 515–528, 1990.
- Wilkars W, Liu Z, Lewis AS, Stoub TR, Ramos EM, Brandt N, Nicholson DA, Chetkovich DM, Bender RA.** Regulation of axonal HCN1 trafficking in perforant path involves expression of specific TRIP8b isoforms. *PLoS One* 7: e32181, 2012.
- Williams SR, Wozny C.** Errors in the measurement of voltage-activated ion channels in cell-attached patch-clamp recordings. *Nat Commun* 2: 242, 2011.
- Zolles G, Klöcker N, Wenzel D, Weisser-Thomas J, Fleischmann BK, Roeper J, Fakler B.** Pacemaking by HCN channels requires interaction with phosphoinositides. *Neuron* 52: 1027–1036, 2006.
- Zolles G, Wenzel D, Bildl W, Schulte U, Hofmann A, Müller CS, Thumfart JO, Vlachos A, Deller T, Pfeifer A, Fleischmann B, Roeper J, Fakler B, Klöcker N.** Association with the auxiliary subunit PEX5R/Trip8b controls responsiveness of HCN channels to cAMP and adrenergic stimulation. *Neuron* 62: 814–825, 2009.

